

Comprehensive evaluation of a benzimidazole-1,3,4-oxadiazole derivative for corrosion protection of C38 steel in HCl: Experimental, molecular dynamics, monte carlo, and in silico pharmacokinetic approaches

Assiya Atif^{a*}, Soukaina Ameer^{a,b}, Ahmed Bendaoud^b, Rachid Hsissou^c, Said Jebbari^a, Houssine Ait Sir^a and Mohammed Salah^b

^aBioorganic Chemistry Team, Laboratory of Bioorganic Chemistry, Faculty of Sciences, Chouaib Doukkali University, 24000 El Jadida, Morocco

^bMolecular Modeling and Spectroscopy Research Team, Faculty of Sciences, Chouaib Doukkali University, 24000 El Jadida, Morocco

^cLaboratory of Organic Chemistry, Bioorganic and Environment, Chemistry Department, Faculty of Sciences, Chouaib Doukkali University, El Jadida, Morocco

CHRONICLE

Article history:

Received March 15, 2025

Received in revised form

June 9, 2025

Accepted August 9, 2025

Available online

August 9, 2025

Keywords:

Synthesis

Characterization

Corrosion inhibitor

DFT

Molecular docking

ADME/Toxicity

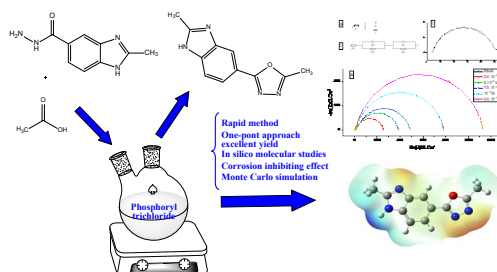
Monte Carlo

Molecular Dynamics

ABSTRACT

In this study, 2-methyl-5-(2-methyl-1H-benzimidazol-5-yl)-1,3,4-oxadiazole, a novel heterocyclic compound derived from 1,3,4-oxadiazole, is synthesised and thoroughly characterised. Mass spectrometry, FTIR-ATR spectroscopy, ¹H-NMR, and ¹³C-NMR were used for structural elucidation. This compound's ability to inhibit corrosion in C38 steel in 1 M hydrochloric acid was examined using both stationary (potentiodynamic polarisation) and non-stationary (electrochemical impedance spectroscopy, EIS) electrochemical techniques. The inhibitor considerably decreased the corrosion current density, as shown by the Tafel polarisation curves, and its effectiveness improved with increasing concentration. Nyquist plots supported these results by showing that charge transfer resistance increased with immersion time, indicating stable surface adsorption and efficient protection. Monte Carlo (MC) and Molecular Dynamics (MD) simulations were performed on the Fe(110) surface in the presence of a simulated acidic aqueous environment in order to obtain molecular-level understanding of the inhibitor's adsorption behaviour. These simulations supported the high inhibition efficiency observed in experiments by confirming strong adsorption energies and stable conformations of the inhibitor on the metallic surface. Moreover, molecular docking studies revealed the compound's multi-target binding affinities, which frequently outperformed reference ligands and indicated the possibility of wider biological applications. Although hepatotoxicity was noted as a possible concern that required additional biological validation, in silico ADME and toxicity profiling showed generally positive pharmacokinetic properties. This multidisciplinary strategy, which combines computational modelling, pharmacological profiling, and experimental electrochemistry, highlights the potential of this benzimidazole–oxadiazole derivative as a dual-purpose corrosion inhibitor and bioactive candidate.

© 2025 by the authors; licensee Growing Science, Canada.



Graphical Abstract

* Corresponding author

E-mail address assis.atif@gmail.com (A. Atif)

© 2025 by the authors; licensee Growing Science, Canada

doi: 10.5267/j.ecl.2025.8.005

1. Introduction

Cyclic organic compounds with at least one heteroatom are known as heterocyclic compounds and can be used in several fields.¹⁻³ Although many heterocyclic rings contain other heteroatoms, the most common ones are nitrogen, oxygen, and sulphur. Because they are involved in a variety of conditions, heterocyclic compounds are regarded as one of the fundamental classes of organic compounds and are utilised in many biological fields.⁴ In the fields of medicinal chemistry, pesticides, polymer science, and materials science.⁵ Oxadiazoles five-membered heterocycles made up of two carbon atoms, two nitrogen atoms, and one oxygen atom are receiving a lot of attention. There are various regioisomeric forms of oxadiazole rings.⁶ Several commercially available compounds contain 1,3,4-oxadiazole, including zibotentan, an experimental anti-cancer drug, furamizol, an antibacterial agent, and raltegravir, an HIV integrase inhibitor that is effective against HIV-14.⁷⁻⁹ (Fig 1).

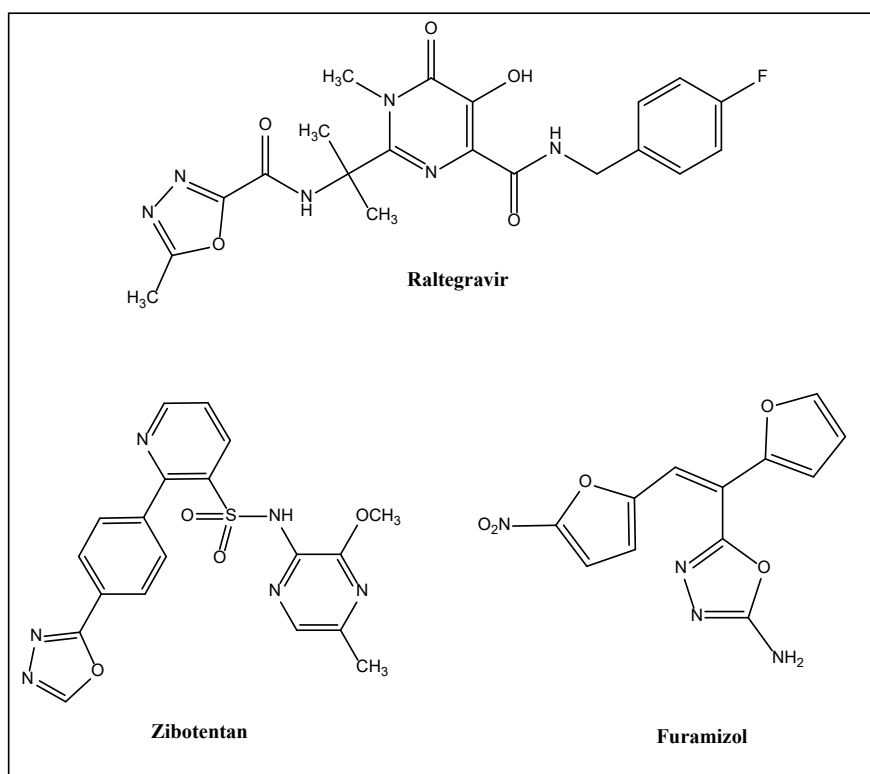


Fig 1. Structure of Raltegravir, Zibotentan and Furamizol.

There are numerous pharmacological uses for 1,3,4-Oxadiazole. Researchers have been creating new compounds with the 1,3,4-oxadiazole core for a number of years. These compounds have shown a wide range of biological activity, including anti-inflammatory properties,¹⁰⁻¹³ analgesic properties,¹⁴ anti-depressive properties,^{15,16} anticancer properties,^{17,18} anti-diabetic properties,^{19,20} antibacterial properties,²¹⁻²³ antifungal properties,^{24,25} and antiviral properties.^{26,27} In order to assess the possible antitubercular, antioxidant/enzyme regulatory, and antifungal properties of 2-methyl-5-(2-methyl-1H-benzimidazol-5-yl)-1,3,4-oxadiazole, in silico methods,²⁸ molecular docking analyses,²⁹⁻³¹ and ADME/toxicity prediction were used.²⁹ In addition to speeding up the process of finding promising candidates, this combined approach provides insightful information about the pharmacokinetic characteristics and molecular interactions of these candidates with biological targets.

The bioactivity of 2-methyl-5-(2-methyl-1H-benzimidazol-5-yl)-1,3,4-oxadiazole is determined by the presence of the nitrogen atom in the heterocyclic molecular segment.³²⁻³⁵

2. Materials and Methods

2.1. Reagents and instruments

All solvents and reagents were obtained from Sigma Aldrich and were used without any further modification. Thin-layer chromatography (TLC) was performed using aluminum sheets coated with Merck 60 F254 silica gel (0.2 mm thickness) to monitor the progress of the reactions. For detection, a UV-visible lamp was employed, with wavelengths set to 254 and 365 nm. The melting points of the synthesized compounds were determined using a Köfler bench, and the values were not

converted into degrees Celsius. FTIR spectra were recorded using a SHIMADZU FT-IR 8400S spectrometer with a total reflection crystal diamond (ATR) accessory, covering a range of 500–4000 cm^{-1} . The Fourier transform JNM-ECZ500/S1 FT NMR SYSTEM (JEOL) at the Centre National pour la Recherche Scientifique et Technique (CNRST) in Rabat was used for the NMR measurements, with a proton frequency of 500 MHz and a carbon frequency of 125 MHz. The solvent used for NMR analysis was DMSO- d_6 , with chemical shifts reported at 2.5 ppm for ^1H NMR and 39.7 ppm for ^{13}C NMR. The Ultimate 3000-Exactive plus THERMO quadrupole-Orbitrap instrument, also available at CNRST, was employed for high-resolution mass spectrometry, equipped with a collision cell.

2.1.1. Synthesis of 2-methyl-1H-benzimidazole-carboxylic acid (2)

A solution of 3,4-diaminobenzoic acid (**1**) (40 mmol) in concentrated hydrochloric acid (30 ml) was mixed with glacial acetic acid (60 mmol). For six hours, the reaction mixture was heated until it refluxed. Following cooling, 25% ammonia was added to the reaction medium to bring its pH down to 4. The resulting precipitate was then filtered and recrystallised from ethanol as a brown powder^{36–38}. Solid brown; 85%; > 300°C, ^1H NMR(500MHz,DMSO- d_6 ,ppm): 2.56(s,3H,CH₃), 7.16(d,1H,CHar), 7.56(s,1H,CHar), 7.87(d,1H,CHar), 10.49(s,1H,NH), 11.00(s,1H,OH), ^{13}C NMR (125MHz,DMSO- d_6 , ppm) : 160.60(C=O), 155.32(C=N), 146.80(Car), 136.44(Car), 127.83(Car), 127.30(Car), 116.84(Car), 115.10(Car), 19.10(CH₃), IR-ATR (cm^{-1}): 3225 $\nu\text{N-H}$, 2962-3218 $\nu\text{O-H}$, 1712 $\nu\text{C=O}$, 1625 $\nu\text{C=N}$, MS(ESI): $m/z = 177$ [M+H]⁺

2.1.2. Synthesis of ethyl 2-methyl-1H-benzimidazole-5-carboxylate (3)

To get ethyl 2-methyl-1H-benzimidazole-5-carboxylate (**3**), 7 mmol After adding 8 ml of thionyl chloride at 0°C to 30 ml of absolute ethanol, 2-methyl-1H-benzimidazole-5-carboxylic acid (**2**) was allowed to reflux for 24 hours. Following the termination of the reaction, a 10% NaHCO₃ solution was used to neutralise the mixture to a pH of 7. A buff-colored powder³⁹ was produced by filtering and recrystallising the precipitate from ethanol. Solid chamois; 79%; 170-172°C, ^1H NMR(500MHz,DMSO- d_6 ,ppm): 1.30(t,3H,CH₃), 2.56(s,3H,CH₃), 4.27(q,2H,CH₂), 7.24(s,1H,CHar), 7.56(d,1H,CHar), 8.00(d,1H,CHar), 11.00(s,1H,NH), ^{13}C NMR (125MHz,DMSO- d_6 , ppm) : 162.86(C=O), 156.66(C=N), 148.35(Car), 135.52(Car), 126.44(Car), 124.14(Car), 116.41(Car), 114.79(Car), 69.00(CH₂), 19.84(CH₃), 19.10(CH₃), IR-ATR (cm^{-1}): 3321 $\nu\text{N-H}$, 1718 $\nu\text{C=O}$, 1632 $\nu\text{C=N}$, MS(ESI): $m/z = 205$ [M+H]⁺

2.1.3. Synthesis of 2-methyl-1H-benzimidazole-5-carbohydrazide (4)

Ethyl 2-methyl-1H-benzimidazole-5-carboxylate (**3**) (7 mmol) and hydrazine hydrate (10 ml) were mixed for 18 hours at room temperature in order to prepare 2-methyl-1H-benzimidazole-5-carbohydrazide (**4**). The solid was recrystallised from ethanol as a brown powder⁴⁰ after the reaction mixture was concentrated and repeatedly triturated with methanol to eliminate excess hydrazine hydrate. Solid brown; 80%; 260-262°C, ^1H NMR(500MHz,DMSO- d_6 ,ppm): 2.74(s,3H,CH₃), 4.86(s,2H,NH₂), 7.37(s,1H,CHar), 7.54(d,1H,CHar), 7.86(d,1H,CHar), 9.28(s,1H,NH), 10.20(s,1H,NH), ^{13}C NMR (125MHz,DMSO- d_6 , ppm): 168.22(C=O), 152.67(C=N), 149.33(Car), 135.29(Car), 130.30(Car), 129.85(Car), 117.42(Car), 116.06(Car), 18.91(CH₃), IR-ATR (cm^{-1}): 3331 $\nu\text{N-H}$, 3212 $\nu\text{N-H}$, 3101-3192 νNH_2 , 1675 $\nu\text{C=O}$, 1596 $\nu\text{C=N}$, MS(ESI): $m/z = 191$ [M+H]⁺

2.1.4. Synthesis of 2-methyl-5-(2-methyl-1H-benzimidazol-5-yl)-1,3,4-oxadiazole (5)

After dissolving 3 mmol of acetic acid in 15 ml of phosphoryl trichloride, adding 3 mmol of 2-methyl-1H-benzimidazole-5-carbohydrazide (**4**), and heating the reaction mixture at reflux for 6 hours, the reaction is complete. The precipitate that formed was filtered and recrystallised from ethanol⁴¹ after the reaction was stopped and the mixture was neutralised with 25% ammonia until pH = 7. Solid beige; 93%; 223-225°C, ^1H NMR(500MHz,DMSO- d_6 ,ppm): 2.51(s,3H,CH₃), 2.56(s,3H,CH₃), 7.16(d,1H,CHar), 7.57(s,1H,CHar), 7.87(d,1H,CHar), 11.00(s,1H,NH), ^{13}C NMR (125MHz,DMSO- d_6 , ppm) : 169.06(C=N), 168.20(C=N), 155.32(C=N), 135.52(Car), 132.98(Car), 130.08(Car), 121.62(Car), 115.51(Car), 114.79(Car), 19.84(CH₃), 19.10(CH₃), IR-ATR (cm^{-1}): 3149 $\nu\text{N-H}$, 1633 $\nu\text{C=N}$, 1286 $\nu\text{C-H}$, MS(ESI): $m/z = 215$ [M+H]⁺

2.2. Experimental conditions

The steel used for the tests was composed of 0.009% cobalt, 0.680% manganese, 0.230% silicon, 0.077% chromium, 0.059% nickel, 0.0160% sulfur, 0.011% titanium, 0.370% carbon, and 98.39% iron. To prepare the C38 steel (SC38 = 1.77 cm^2) for testing, SiC paper of grades 180, 600, and 1200 was utilized for polishing, followed by rinsing with distilled water, ultrasonic cleaning with ethanol, and drying. The efficiency of inhibitor adsorption was found to be influenced by the surface preparation, as roughness affects the process. The inhibitor molecule was used in this study at concentrations ranging from 2.5×10^{-5} to 2.5×10^{-4} M, dissolved in 80 mL of 1 M HCl at ambient temperature. Electrochemical measurements, including Electrochemical Impedance Spectroscopy (EIS) and Potentiodynamic Polarization (PDP), were carried out using the VMP3 potentiostat connected to EC-Lab software. The measurement system consisted of three electrodes: a Saturated Calomel Electrode (SCE) as the reference, a platinum wire as the auxiliary electrode, and C38 steel as the working electrode. Stable electrochemical testing conditions were ensured by potential stabilization, with EIS data collected over a frequency

range of 100 kHz to 10 mHz. For the PDP polarization curves, the applied potential was varied continuously at a rate of 0.5 mV/s within a potential window of ± 250 mV.

2.3. Simulation-Based Methods and Molecular Modeling Approaches

To comprehensively investigate the interaction mechanisms between organic inhibitors and metallic surfaces in corrosive environments, a combination of quantum chemical calculations, molecular docking, and classical simulation techniques was employed. Molecular optimization of the inhibitor structures was performed using Gaussian 09⁴², with GaussView 6 serving as the graphical interface for visualization and preparation. Protein structures were retrieved from the Protein Data Bank (PDB)⁴³, and reference ligands were obtained from PubChem⁴⁴. Molecular docking was conducted using AutoDock Tools⁴⁵ in conjunction with AutoDock Vina⁴⁶, enabling the prediction of ligand-receptor affinities and binding conformations. Docking preparations and PDBQT file generation were facilitated by Discovery Studio, which, along with Maestro Schrödinger, was also used for advanced visualization and analysis. To extend the scope of static docking results and capture the dynamic behavior of the inhibitor in realistic environments, Molecular Dynamics (MD) and Monte Carlo (MC) simulations were performed. These complementary computational techniques enabled a detailed evaluation of adsorption properties, energetics, and intramolecular interactions, particularly in the presence of solvated ions representative of acidic media. Among various crystallographic configurations of iron, the Fe (110) surface was selected for its stability and relevance to corrosion studies. The surface was extended into a supercell to maximize the area available for interaction, and a simulation box with dimensions $30.18 \times 42.42 \times 45.57 \text{ \AA}^3$ and periodic boundary conditions was defined. A vacuum layer of 15 \AA was incorporated above the metallic slab to eliminate inter-image interactions. The modeled system included one inhibitor molecule (AM02), 15 hydronium ions (H_3O^+), 15 chloride ions (Cl^-), and 163 water molecules (H_2O), reproducing a realistic acidic aqueous environment. The MD simulations were carried out under an NVT ensemble, with the Andersen thermostat regulating the system's temperature. Simulations were conducted at two temperatures (203 K and 343 K) using the COMPASS force field, a 1 fs timestep, and a total simulation duration of 50 ps. The interaction and binding energies were calculated using the following equations:

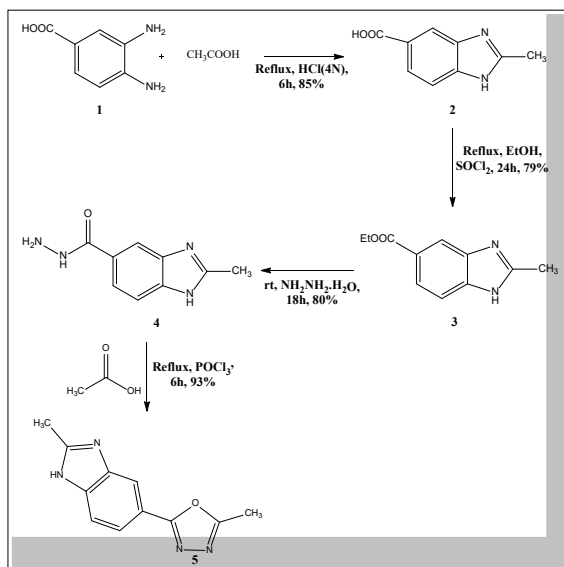
$$E_{int} = E_{complex} - (E_{inh} + E_{Fe+163H_2O+15Cl^-+15H_3O^+}) \quad (1)$$

$$E_{bind} = -E_{int} \quad (2)$$

3. Results and Discussion

3.1. Synthesis of 2-methyl-5-(2-methyl-1H-benzimidazol-5-yl)-1,3,4-oxadiazole (5)

By using the Phillips method^{36–38} to condense 3,4-diaminobenzoic acid (OPDA) with acetic acid in hydrochloric acid, 2-Methyl-1H-benzimidazole-5-carboxylic acid (**2**) was produced in a good yield. Our working strategy involved the esterification of 2-methyl-1H-benzimidazole-5-carboxylic acid (**2**), which involves activating the carboxylic acid at reflux for 24 hours³⁹ using ethanol and thionyl chloride. After that, hydrazine hydrate is applied to the esterified product (**3**) for eighteen hours at room temperature. Following treatment, an 80% yield of 2-methyl-1H-benzimidazole-5-carbohydrazide (**4**) is produced. The process of reacting 2-methyl-1H-benzimidazole-5-carbohydrazide (**4**) with acetic acid in the presence of phosphoryl trichloride at reflux was selected to produce 2-methyl-5-(2-methyl-1H-benzimidazol-5-yl)-1,3,4-oxadiazole (**5**). Following ammonia neutralisation of the reaction mixture to a pH of neutral, a precipitate is created, filtered, and recrystallised from ethanol⁴¹ (**Scheme 1**).



Scheme 1. Synthesis of 2-methyl-5-(2-methyl-1H-benzimidazol-5-yl)-1,3,4-oxadiazole

Two singlets with three methyl protons each at 2.51 and 2.56 ppm, a deshielded signal from the benzimidazole proton at 11.00 ppm, and clusters with aromatic protons between 7.16 and 7.87 ppm are all visible in the compound's ^1H NMR spectrum. In the compound's ^{13}C NMR spectrum, the methyl carbons are responsible for two signals at 19.10 and 19.84 ppm, the C=N bonds for three signals at 169.06, 168.20, and 155.32 ppm, and the aromatic carbons for signals at 135.52, 132.98, 130.08, 121.62, 115.51 and 114.79 ppm. Three bands are visible in the spectrum: the N-H of benzimidazole at 3149 cm^{-1} , the C=N bond at 1633 cm^{-1} , and the C-H bond of methyl at 1286 cm^{-1} .

A molecular peak associated with the molecular ion $m/z = 215[\text{M}+\text{H}]^+$ can be seen in the mass spectrum captured in (ESI).

3.2. ADME/Toxicity Analysis and Molecular Docking Study

3.2.1. ADME Properties Predicted by pKCSM

The pKCSM prediction platform was employed to perform an in silico ADME (Absorption, Distribution, Metabolism, and Excretion) analysis to evaluate the pharmacokinetic properties of the designed compound. This computational approach estimates essential drug-like properties that influence how a molecule behaves within a biological system. The ADME predictions provide an early assessment of the compound's potential as a drug candidate by highlighting its oral bioavailability, tissue distribution, metabolic stability, and clearance.

According to the ADME profile, the compound demonstrates good intestinal absorption, acceptable CaCO_2 permeability, and favorable oral bioavailability. It also reduces the likelihood of drug-drug interactions since, despite being a substrate for P-glycoprotein, it does not inhibit the transporter. However, the compound shows poor permeability through the Central Nervous System (CNS) and Blood-Brain Barrier (BBB), which could mitigate central side effects for non-neuroactive drugs. The metabolism prediction indicates minimal interaction with key CYP450 enzymes, thereby decreasing the risk of metabolic issues. Additionally, the compound exhibits a balanced pharmacokinetic profile, supported by moderate total clearance and non-OCT2-mediated renal excretion.

Regarding the toxicity profile, the compound is generally safe. It does not pose a risk for cardiotoxicity via hERG inhibition and is not mutagenic. In animal models, it exhibits low acute oral toxicity and shows no potential for skin sensitization. However, hepatotoxicity was predicted, warranting caution and further in vitro/in vivo testing. Its environmental compatibility is also favorable, as evidenced by its low ecological toxicity (**Table 1S**, and **Table 2S** see supplementary data).

3.2.2. Prediction of Biological Interactions via Molecular Docking

The molecular docking study aimed to evaluate the binding affinity of the designed ligand to three physiologically relevant target proteins: antitubercular, antioxidant/enzymatic regulation, and antifungal targets. The results were compared with standard reference ligands known to be active against these targets (**Table 1**).

When docked with InhA (PDB: 4YZK), an important enzyme in *Mycobacterium tuberculosis*, the ligand exhibited a binding affinity of -5.1 kcal/mol for antitubercular activity, surpassing the reference drug isoniazid, which had a binding affinity of -4.1 kcal/mol . This suggests that the ligand could possess superior or more competitive inhibitory activity against InhA.

For antioxidant and enzymatic regulation, the ligand showed a significantly higher binding affinity of -6.8 kcal/mol with Tyrosinase (PDB: 2Y9X), compared to the reference compound Kojic acid (-5.3 kcal/mol). This enhanced binding indicates that the ligand may form stronger hydrogen bonds or hydrophobic interactions at the active site, potentially leading to more effective inhibition of tyrosinase. In terms of antifungal activity, the ligand outperformed the established antifungal drug Fluconazole, which had a docking score of -7.4 kcal/mol , achieving a score of -7.8 kcal/mol with Lanosterol 14 α -demethylase (CYP51) (PDB: 5EQB). This suggests that the ligand may be a potent inhibitor of fungal CYP51, a key enzyme in the biosynthesis of fungal membranes. Across all tested targets, the ligand demonstrated favorable binding energies, often outperforming the reference drugs. These findings imply that the ligand could have broad-spectrum therapeutic potential and warrants further investigation, including biological validation and ADMET profiling.

Table 1. Comparative Docking Affinities of the Ligand and Reference Ligands for Different Therapeutic Activities

Biological Activity	Target Protein	PDB ID	Ligand	Binding Affinity (kcal/mol)
Antitubercular	InhA (<i>Mycobacterium tuberculosis</i>)	4YZK	Isoniazid	-4.1
			Ligand	-5.1
Antioxidant / Enzymatic Regulation	Tyrosinase	2Y9X	Kojic Acid	-5.3
			Ligand	-6.8
Antifungal	Lanosterol 14 α -demethylase (CYP51)	5EQB	Fluconazole	-7.4
			Ligand	-7.8

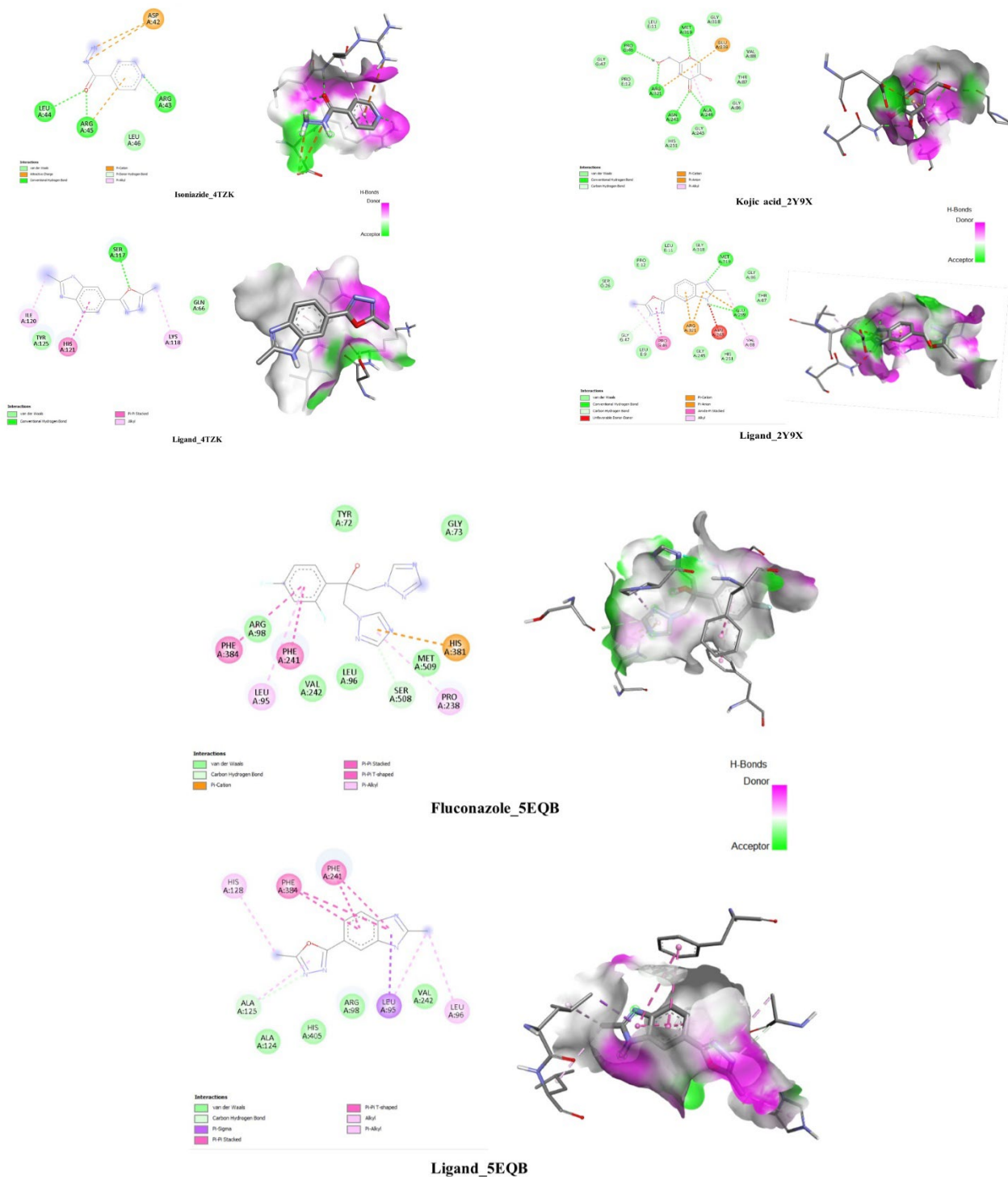


Fig. 4. 2D and 3D interaction profiles of our ligand and reference Fluconazole with the active sites of the protein Lanosterol 14 α -demethylase (CYP51) (5EQB).

In the active sites of three therapeutic targets, the interaction profiles show the precise binding modes of the designed ligand in comparison to reference compounds. The ligand exhibits a more extensive interaction network than isoniazid within the InhA enzyme (PDB: 4YZK) by establishing a number of non-covalent interactions, including van der Waals forces, conventional hydrogen bonds, π - π stacking, and alkyl interactions. Tyrosinase (PDB: 2Y9X) has a more complex and possibly stable binding conformation than Kojic acid because the ligand shows other bonding types, such as carbon-hydrogen bonds, π -anion interactions, and even some unfavourable donor-donor contacts. The ligand exhibits strong π -sigma interactions, hydrogen bonds, and hydrophobic contacts when bound to Lanosterol 14 α -demethylase (CYP51, PDB: 5EQB), which contributes to its increased affinity over fluconazole. The ligand's potential in a variety of therapeutic domains is strengthened by these molecular interactions, which facilitate its efficient engagement with various protein targets.

3.3. Corrosion inhibitory activity for C38 steel in hydrochloric acid (1M HCl)

3.3.1. Potentiodynamic polarization (PPD) curves

To better understand the kinetics of cathodic and anodic corrosion reactions, Tafel diagrams were examined⁴⁷. Following a 30-minute immersion in an acidic medium (1M HCl) at 298 K, **Fig. 5** displays the potentiodynamic polarisation curves of C38 steel with and without varying concentrations of 2-methyl-5-(2-methyl-1H-benzimidazol-5-yl)-1,3,4-oxadiazole. The Tafel slope⁴⁸ is used to calculate the electrochemical parameters of C38 steel without and with varying concentrations of 5f, including corrosion potential (E_{corr}), corrosion current density (i_{corr}), cathodic Tafel constant (β_c), and inhibitory efficiency (η_{PPD} (%)) (**Table 2**).

When varying concentrations of the inhibitor molecule are added to the corrosive solution, the corrosion potential slightly shifts towards more negative values in comparison to the control (1M HCl). Furthermore, the cathodic slopes change to correspondingly lower values. As a result, corrosion currents decrease, which in turn indicates a decrease in corrosion rates^{49,50}. The cathodic Tafel lines and cathodic slopes for 2-methyl-5-(2-methyl-1H-benzimidazol-5-yl)-1,3,4-oxadiazole are nearly parallel and roughly constant, respectively (**Fig. 5** and **Table 2**). This suggests that the tested inhibitor molecule⁵¹ has no effect on the cathodic reactions of the electrode corrosion mechanisms of C38 steel. Equations 1 and 2 also show the electrochemical reactions of C38 steel in an acid solution (1M HCl), which correspond to the cathodic (hydrogen reduction) and anodic (iron dissolution) reactions. Equation 3 was used to calculate the inhibitory efficiency.



$$\eta_{PPD} (\%) = \left(1 - \frac{i_{inh}}{i_0}\right) \times 100 \quad (3)$$

The corrosion current densities without and with varying concentrations of the tested inhibitor (2-methyl-5-(2-methyl-1H-benzimidazol-5-yl)-1,3,4-oxadiazole) are denoted by i_0 and i_{inh} , respectively. As the concentration of the inhibitor molecule (2-methyl-5-(2-methyl-1H-benzimidazol-5-yl)-1,3,4-oxadiazole) in the corrosive solution increases, the cathodic corrosion current densities decrease significantly. This suggests that the cathodic reactions⁵² can also be impacted by the 2-methyl-5-(2-methyl-1H-benzimidazol-5-yl)-1,3,4-oxadiazole used. As can be seen in **Table 2**, at 2.5×10^{-4} Mol/L of (2-methyl-5-(2-methyl-1H-benzimidazol-5-yl)-1,3,4-oxadiazole) investigated in the corrosive solution, the corrosion current densities drop and reach extremely low values of the order of $11.4 \mu A cm^{-2}$. This suggests that the 2-methyl-5-(2-methyl-1H-benzimidazol-5-yl)-1,3,4-oxadiazole is $520.1 \mu A cm^{-2}$ in comparison to the control (1M HCl). A thorough examination of **Table 2** reveals that as the concentration of the inhibitor molecule under test increases, the corrosion current densities decrease. However, the inhibitory efficiencies rise as the concentration of 2-methyl-5-(2-methyl-1H-benzimidazol-5-yl)-1,3,4-oxadiazole increases. At an ideal concentration of 2.5×10^{-4} Mol/L, the inhibitory efficiencies reach a maximum value of the order of 97.81%. This suggests that 2-methyl-5-(2-methyl-1H-benzimidazol-5-yl)-1,3,4-oxadiazole is an effective inhibitor. It contains an aromatic ring and two heterocyclic rings that carry the following heteroatoms: oxygen and nitrogen. These heteroatoms adsorb on the metal surface in a parallel and plane fashion, forming a protective film on the steel electrode's surface.^{53, 54}

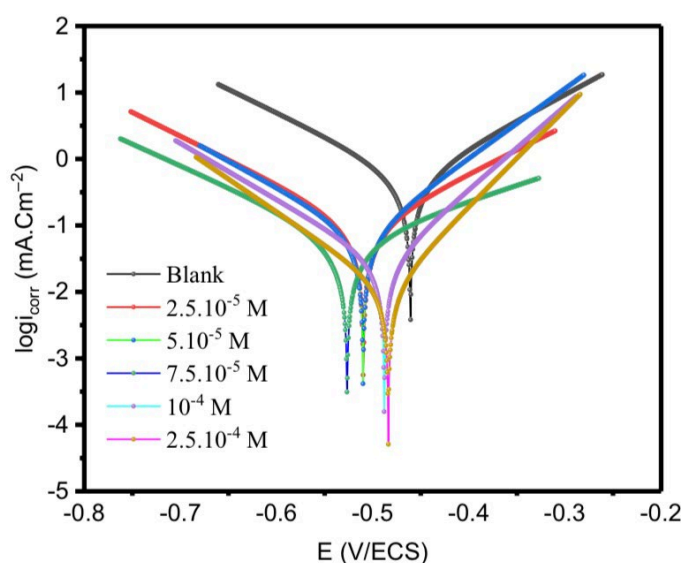


Fig 5. Potentiodynamic polarization curves of C38 steel in the absence and presence of the tested inhibitor (2-methyl-5-(2-methyl-1H-benzimidazol-5-yl)-1,3,4-oxadiazole) at different concentrations in 1M HCl solution at 298 K.

Table 2. Different electrochemical parameters of C38 steel in the absence and presence of the tested inhibitor (2-methyl-5-(2-methyl-1H-benzimidazol-5-yl)-1,3,4-oxadiazole) at different concentrations in 1M HCl at 298 K.

Concentration (Mol/L)	i_{corr} ($\mu\text{A}\cdot\text{cm}^{-2}$)	$-E_{corr}$ (mV/SCE)	β_a (mV)	$-\beta_c$ (mV)	EI (%)
Blank	520.1	460.7	128.4	142.2	-
$2.5\cdot 10^{-5}$	96.3	509.7	138.5	140.0	81.48
$5\cdot 10^{-5}$	72.6	509.9	95.6	126.6	86.04
$7.5\cdot 10^{-5}$	59.7	526.6	213.0	154.3	88.52
10^{-4}	27.4	487.8	79.7	118.1	94.73
$2.5\cdot 10^{-4}$	11.4	483.7	68.4	101.3	97.81

3.3.2. Electrochemical impedance spectroscopy (EIS)

Electrochemical impedance spectroscopy (EIS) was used to investigate the interaction and impact of the tested inhibitor (2-methyl-5-(2-methyl-1H-benzimidazol-5-yl)-1,3,4-oxadiazole) on the electrode surface of C38 steel in a corrosive environment, in order to validate the results previously obtained using potentiodynamic polarisation curves. Furthermore, EIS was employed to assess corrosion resistance and comprehend the organic inhibitor's adsorption mechanisms in both the uninhibited and inhibited aggressive solutions⁵⁵. **Fig. 6** displays the Nyquist diagrams of C38 steel following a 30-minute immersion in 1M HCl at 298 K, both with and without varying concentrations of 2-methyl-5-(2-methyl-1H-benzimidazol-5-yl)-1,3,4-oxadiazole. When compared to the control capacitive loop (without inhibitor), the diameter of the capacitive loops increases with increasing concentration, according to the Nyquist diagrams of the SIE in the corrosive solution with and without varying concentrations of 2-methyl-5-(2-methyl-1H-benzimidazol-5-yl)-1,3,4-oxadiazole⁵⁶. Additionally, the charge transfer resistance and low-frequency scattering associated with the adsorption of the organic inhibitor molecule 2-methyl-5-(2-methyl-1H-benzimidazol-5-yl)-1,3,4-oxadiazole on the metal surface at the metal/solution interface⁵⁷ cause the shape and size of Nyquist diagrams to change when varying concentrations of the inhibitor molecule are added to the aggressive medium. This shows that the Cl⁻ ion attack has been halted and that the protective layer that has formed is firmly attached to the metal surface. This implies that C38 steel in an acidic medium exhibits a very high resistance to varying concentrations of the investigated molecule, and that the inhibitory efficiency rises as the concentration of 2-methyl-5-(2-methyl-1H-benzimidazol-5-yl)-1,3,4-oxadiazole increases. Due to the adhesion of the tested organic molecule and the creation of hydrogen and covalent bonds between the C38 steel surface and the lone pairs of heteroatoms (nitrogen and oxygen) as well as the double bonds of aromatic rings^{58,59}, these results can be explained. The various electrochemical parameters that were taken from the Nyquist diagrams that were simulated using an equivalent electrical circuit (EEC) with and without varying concentrations of 2-methyl-5-(2-methyl-1H-benzimidazol-5-yl)-1,3,4-oxadiazole (**Fig. 3**) are listed in **Table 3**. Furthermore, the solution resistance (R_s), charge transfer resistance (R_{ct}), and constant phase element (CPE) make up the majority of the EEC. Equations 4 and 5⁶⁰ were then used to determine the inhibitor 2-methyl-5-(2-methyl-1H-benzimidazol-5-yl)-1,3,4-oxadiazole's double layer capacity (C_{dl}) and inhibitory efficiency (η_{SIE} (%)). Due to the complete adsorption of 2-methyl-5-(2-methyl-1H-benzimidazol-5-yl)-1,3,4-oxadiazole and the development of a protective film on the steel surface, this result indicates that 2-methyl-5-(2-methyl-1H-benzimidazol-5-yl)-1,3,4-oxadiazole is the best inhibitor tested. Furthermore, potentiodynamic polarisation is confirmed by the results of the electrochemical impedance spectroscopy method. Furthermore, these findings are consistent with those of other researchers who have published their findings in the literature^{61,62}.

$$C_{dl} = Y_0(\omega_m)^{n-1} \quad (4)$$

$$\eta_{SIE} (\%) = \left(1 - \frac{R_{ct}^0}{R_{ct}}\right) \times 100 \quad (5)$$

With R_{ct}^0 and R_{ct} are respectively the charge transfer resistance in the absence and presence of different concentrations of the tested inhibitor (2-methyl-5-(2-methyl-1H-benzimidazol-5-yl)-1,3,4-oxadiazole). In addition, Y_0 , ω_m and n present respectively the angular frequency, the CPE amplitude and the exponent.

Table 3. Different electrochemical parameters of C38 steel in the absence and presence of the studied inhibitor (2-methyl-5-(2-methyl-1H-benzimidazol-5-yl)-1,3,4-oxadiazole) at different concentrations in 1M HCl solution at 298 K.

Concentration (Mol/L)	R_1 ($\Omega\cdot\text{cm}^2$)	R_2 ($\Omega\cdot\text{cm}^2$)	R_3 ($\Omega\cdot\text{cm}^2$)	Q_2 ($e^{-3}\cdot\text{F}\cdot\text{cm}^2$)	n_2	Q_3 ($e^{-3}\cdot\text{F}\cdot\text{cm}^2$)	n_3	R_{ct} ($\Omega\cdot\text{cm}^2$)	IE (%)
Blank	4.22	36.5	-	0.323	0.83	-	-	47.83	-
$2.5\cdot 10^{-5}$	5.61	22.31	227	0.739	0.72	0.225	0.88	249.31	80.81
$5\cdot 10^{-5}$	6.64	25.65	353.5	0.908	0.66	0.257	0.85	379.15	87.38
$7.5\cdot 10^{-5}$	6.68	31.46	450.6	0.867	0.65	0.271	0.84	482.06	90.08
10^{-4}	5.681	698	79.98	0.057	0.88	0.518	0.69	777.98	93.85
$2.5\cdot 10^{-4}$	6.331	63.86	1 058	0.289	0.79	0.034	0.88	1121.86	95.74

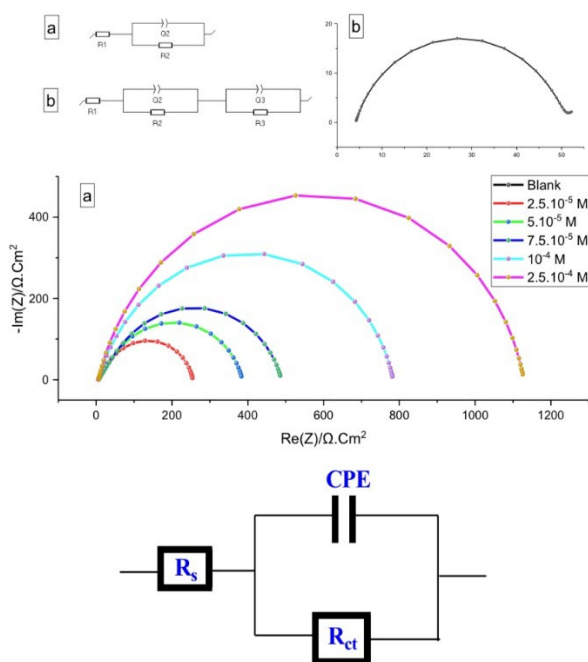


Fig 6. Nyquist diagrams of C38 steel in the absence and presence of the tested inhibitor (2-methyl-5-(2-methyl-1H-benzimidazol-5-yl)-1,3,4-oxadiazole) at different concentrations in 1M HCl solution at 298 K and the equivalent electrical circuit.

3.3.3. Time effect

An effective method for evaluating the corrosion inhibition process by the impact of time (long-term immersion) is electrochemical impedance spectroscopy. The purpose of these experiments is to see how the phenomena at the metal substrate interface change over the course of 2, 4, 6, 8, 16, and 24 hours of immersion. The evolution of the impedance diagrams at various immersion times in 1 M HCl with and without the inhibitor 2-methyl-5-(2-methyl-1H-benzimidazol-5-yl)-1,3,4-oxadiazole at 2.5×10^{-4} M is depicted in **Fig. 7** and **Fig. 8** below. These figures show that after six hours, the charge transfer resistance rises as the immersion time increases. Furthermore, this behaviour suggests that the protective film's resistance has increased for up to 24 hours. As a result, the immersion period improves the film's protective qualities on the steel surface. Furthermore, a very long immersion period is likely to cause the developed passive film to dissolve.

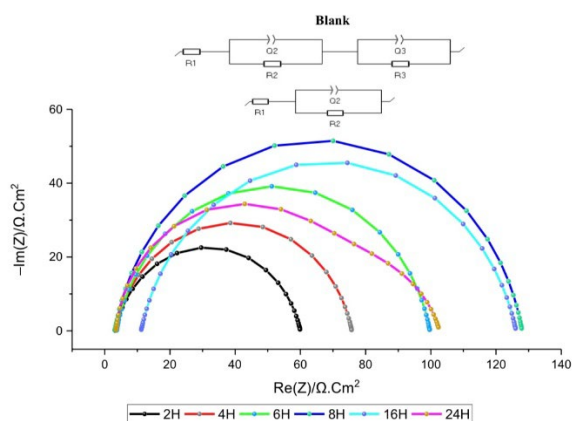


Fig. 7. The evolution of impedance diagrams at different immersion times in 1 M HCl in the absence of the inhibitor 2-methyl-5-(2-methyl-1H-benzimidazol-5-yl)-1,3,4-oxadiazole at 2.5×10^{-4} M.

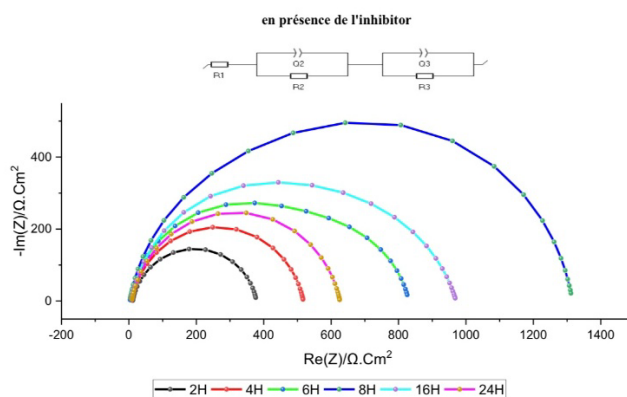


Fig. 8. The evolution of impedance diagrams at different immersion times in 1 M HCl in the presence of the inhibitor 2-methyl-5-(2-methyl-1H-benzimidazol-5-yl)-1,3,4-oxadiazole at 2.5×10^{-4} M.

Table 4. The evolution of impedance diagrams at different immersion times in 1 M HCl in the absence and presence of the inhibitor 2-methyl-5-(2-methyl-1H-benzimidazol-5-yl)-1,3,4-oxadiazole at 2.5×10^{-4} M.

Temps d'immersion	R ₁ ($\Omega \cdot \text{cm}^2$)	R ₂ ($\Omega \cdot \text{cm}^2$)	R ₃ ($\Omega \cdot \text{cm}^2$)	Q ₂ ($\text{e}^{-3} \cdot \text{F} \cdot \text{cm}^{-2}$)	n ₂	Q ₃ ($\text{e}^{-3} \cdot \text{F} \cdot \text{cm}^{-2}$)	n ₃	R _{ct} ($\Omega \cdot \text{cm}^2$)	IE %
Blank									
2	3.146	56.84	-	0.344	0.8	-	-	56.84	-
4	3.255	72.51	-	0.344	0.8	-	-	72.51	-
6	3.642	96.07	-	0.347	0.8	-	-	96.07	-
8	3.102	124.9	-	0.331	0.8	-	-	124.9	-
16	11.16	115	-	0.268	0.8	-	-	115	-
24	3.444	65.28	33.85	0.232	0.9	5.294	0.8	99.11	-
La molécule 5f									
2	11.09	277.2	90.05	0.122	0.8	0.648	0.9	367.25	84.52
4	8.262	162	347.3	0.200	0.9	0.170	0.8	509.3	85.76
6	3.238	342	484.9	0.147	0.8	0.028	0.9	826.9	88.38
8	2.847	353.9	958.9	0.049	0.9	0.062	0.9	1312.8	90.48
16	6.478	534.8	429.5	0.133	0.8	0.055	0.9	964.3	88.07
24	8.368	551.2	66.54	0.018	0.8	0.287	0.9	617.74	83.95

3.4 Monte Carlo simulation, MD results, Fukui Indices, and MEP

3.4.1 Monte Carlo simulation, and MD results

The Monte Carlo simulation results (**Table 5**), and (**Fig. 9**) reveal valuable insights into the adsorption behavior of the inhibitor on the Fe (110) surface. The total energy of the system is -899.031 kJ/mol, indicating overall thermodynamic stability. The adsorption energy is highly negative at approximately -4160 kJ/mol, suggesting a strong exothermic interaction between the inhibitor and the metallic surface, which implies a highly favorable adsorption process. The rigid adsorption energy is recorded at -961.852 kJ/mol, representing the energy associated with adsorption without any structural relaxation of the inhibitor. This value reflects the contribution of non-covalent interactions such as electrostatic and van der Waals forces. The deformation energy of approximately -3200 kJ/mol highlights the significant structural adjustments undergone by the inhibitor during adsorption. This indicates that chemisorption may be involved, where the molecule adapts its conformation to form stable bonds with the surface. Finally, the energy per adsorption site values for specific groups MBO (-126.515), water (-20.608), and hydronium/chloride ions (-13.738) demonstrate that the inhibitor contributes most substantially to the total adsorption energy, confirming its high affinity and effectiveness as a corrosion inhibitor in acidic environments.

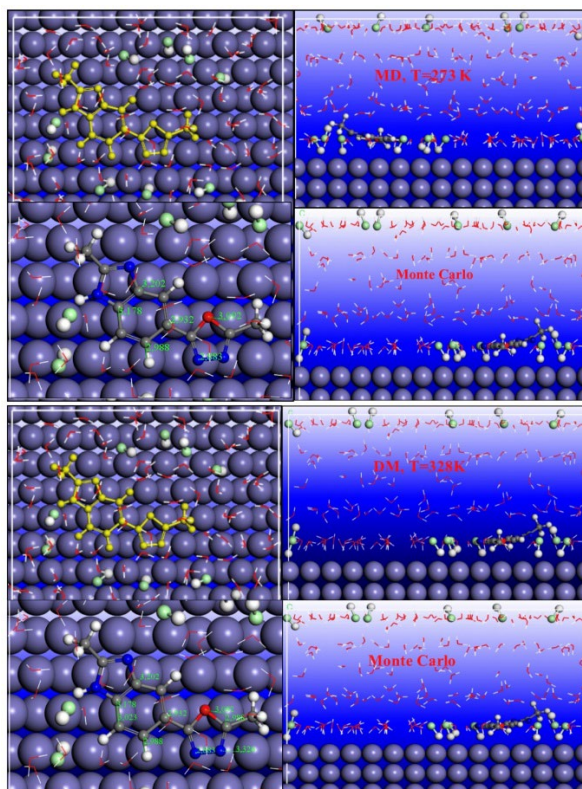


Fig. 9. Comparative Adsorption Behavior of an Organic Inhibitor on Fe(110) Surface at 273 K and 328 K: Molecular Dynamics vs. Monte Carlo Simulations

The Molecular Dynamics (MD) results (**Table 6**), and (**Fig. 9**) at 298 K and 328 K provide additional insights into the system's thermodynamic and structural behavior under dynamic conditions. At 298 K, the interaction energy is negative (-71.217 kJ/mol), indicating a spontaneous and favorable binding of the inhibitor, whereas at 328 K the interaction becomes slightly positive (52.861 kJ/mol), reflecting a possible reduction in binding strength due to increased thermal agitation. Interestingly, the binding energy transitions from positive (71.217 kJ/mol) to negative (-52.861 kJ/mol) as temperature increases, supporting the idea of weakened adsorption at higher temperatures. At both temperatures, the molecule adsorbs in a planar conformation, forming stable interactions with the metallic substrate. The MD simulations reveal temperature-dependent solvent structuring, where water molecules form ordered layers at lower temperatures and become increasingly disordered at 328 K, suggesting thermal destabilization of the solvation shell. Monte Carlo simulations capture thermodynamically favorable configurations, showing consistent surface attachment regardless of temperature. The combination of these static and dynamic methods highlights how temperature influences adsorption strength, molecular conformation, and solvent organization, offering a comprehensive understanding of the inhibitor's performance and its potential application in corrosion protection under varying environmental conditions.

Table 5. Monte Carlo simulation results

Structures	Total energy	Adsorption energy	Rigid adsorption energy	Deformation energy	MBO : dEad/dNi	H2O : dEad/dNi	H3O+ et Cl- : dEad/dNi
Fe (1 1 0)	-899.031	-4.16E+03	-961.852	-3.20E+03	-126.515	-20.608	-13.738

Table 6. Molecular Dynamic results

T(K)	298	328
$E_{\text{complex}}(\text{Kj/mol})$	-67859.382	-67645.617
$E_{\text{Fe}+163\text{H}_2\text{O}+15\text{Cl}^{-}+15\text{H}_3\text{O}^{+}}(\text{Kj/mol})$	-67888.604	-67803.35
MBO(Kj/mol)	100.439	104.872
$E_{\text{interaction}}(\text{Kj/mol})$	-71.217	52.861
$E_{\text{binding}}(\text{Kj/mol})$	71.217	-52.861

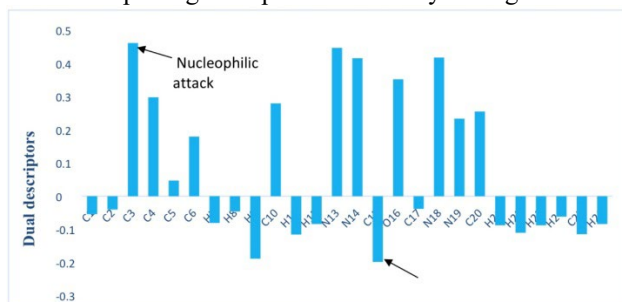
3.4.2 Fukui indices, and Molecular Electrostatic Potential (MEP)

Local reactivity is a widely used method to identify active sites within an inhibitor molecule. In this study, Fukui functions were applied to determine optimal adsorption sites in the optimized structure of the MBO molecule. The following equations were used to calculate the nucleophilic (f_k^+) and electrophilic (f_k^-) Fukui indices:

$$f_k^+ = q(N+1) - q(N) \quad (6)$$

$$f_k^- = q(N) - q(N-1) \quad (7)$$

The analysis of dual descriptors enables the identification of the most reactive atomic sites within the molecule by indicating their propensity for electrophilic or nucleophilic attack. In the plotted data (**Fig. 10**), positive values denote sites likely to undergo nucleophilic attack, whereas negative values suggest susceptibility to electrophilic attack. Notably, the carbon atom C2 exhibits the highest positive dual descriptor value (+0.46), designating it as the principal site for nucleophilic interaction. Other atoms showing significant nucleophilic character include N13 (+0.45), N14 (+0.44), N18 (+0.39), C3 (+0.30), and C10 (+0.28). Additionally, C5 (+0.19), C20 (+0.24), and N19 (+0.23) also demonstrate moderate reactivity toward nucleophilic species. Conversely, O16 stands out with a strongly negative value (-0.26), identifying it as the most electrophilic site, potentially vulnerable to nucleophilic attack. Other atoms such as H8 (-0.22) and H21 to H26, although less reactive, also exhibit slight negative values, consistent with their expected low chemical reactivity. The remaining atoms display values closer to zero, indicating limited reactive behavior. This detailed mapping of reactive centers is essential for predicting molecular behavior in chemical reactions and supports the rational design of compounds in fields such as medicinal chemistry and catalysis. The data are grounded in conceptual density functional theory (DFT), which provides a robust theoretical basis for interpreting site-specific reactivity through dual descriptors.



The reactivity profile of the studied molecule was assessed through a combination of dual descriptor analysis and molecular electrostatic potential (MEP) mapping, providing complementary insights into its electronic structure (**Fig. 11**). The dual descriptor analysis, grounded in conceptual density functional theory (DFT), revealed that carbon atom C2 possesses the highest positive value (+0.46), identifying it as the primary site susceptible to nucleophilic attack. Additional nucleophilic centers include N13 (+0.45), N14 (+0.44), and N18 (+0.39), while O16 exhibited the most negative value (−0.26), suggesting its role as a potential site for electrophilic interaction. These theoretical findings are corroborated by the MEP map, which visualizes the spatial distribution of the molecule's electrostatic potential. The red region, indicating a zone of high electron density, is localized around the oxygen atom, reinforcing its electrophilic nature as predicted. Conversely, blue regions appear on the periphery, particularly near electron-deficient hydrogen atoms, aligning with areas of positive electrostatic potential and potential nucleophilic susceptibility. The green to white gradient over the hydrocarbon backbone suggests regions of lower reactivity. Together, these analyses provide a coherent depiction of the molecule's reactive landscape, enabling a deeper understanding of its potential behavior in electrophilic and nucleophilic environments an essential step in rational drug design and molecular interaction prediction.

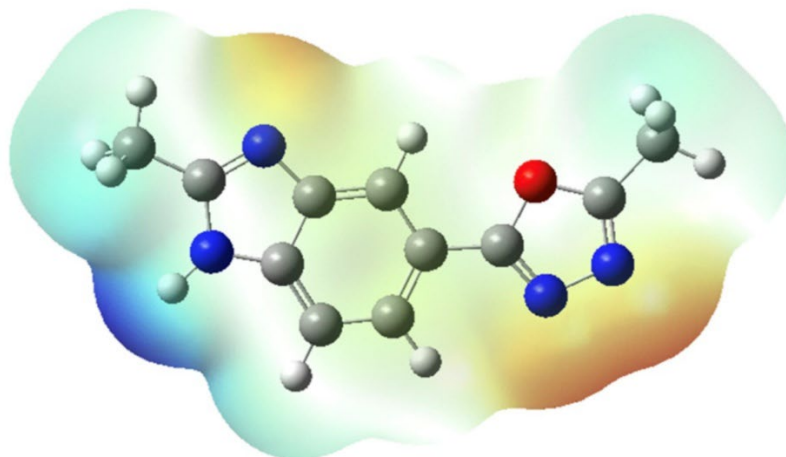


Fig. 11. Molecular Electrostatic Potential (MEP) Map of the Inhibitor Molecule (blue: nitrogen, red: oxygen, gray: carbon, white: hydrogen)

4. Conclusion

This study uses spectroscopic techniques like ^1H NMR, ^{13}C NMR, FTIR-ATR, and mass spectrometry to synthesise and fully characterise 2-methyl-5-(2-methyl-1H-benzimidazol-5-yl)-1,3,4-oxadiazole, a novel heterocyclic compound derived from 1,3,4-oxadiazole. Both stationary and non-stationary electrochemical techniques were used to examine the compound's physicochemical behaviour as a possible corrosion inhibitor for C38 steel in 1 M hydrochloric acid (HCl). The inhibitor dramatically lowers corrosion current densities as concentration rises, according to the stationary technique based on potentiodynamic polarisation (Tafel diagrams). At an ideal concentration of 2.5×10^{-4} mol/L, inhibition efficiencies reach a maximum of 97.81%. These results were validated by the non-stationary approach, which was assessed using electrochemical impedance spectroscopy (EIS): The adsorption of the organic molecule on the steel surface and the creation of a protective film resulted in increased charge transfer resistance, as demonstrated by Nyquist diagrams, which also showed an increase in the diameter of the capacitive loops with increasing inhibitor concentrations. Effective surface coverage and a diffusion-controlled process are further supported by the observed changes in Nyquist plot size and shape, especially at low frequencies. The stability and persistence of the inhibitor on the metal surface were further confirmed by time-dependent EIS measurements, which showed a favourable increase in charge transfer resistance with extended immersion (up to 6 hours). The adsorption behaviour of the inhibitor molecule on the Fe(110) crystallographic plane in an acidic aqueous environment was assessed using Monte Carlo (MC) and Molecular Dynamics (MD) simulations in order to deepen and validate the experimental findings. Using the COMPASS force field in an NVT ensemble, the MD simulations demonstrated robust and stable inhibitor adsorption, with the development of a compact adsorption layer and advantageous interaction energies at both low and high temperatures. The inhibitor-metal complex's thermodynamic stability was further validated by the MC calculations, which produced extremely negative total and adsorption energies that point to a spontaneous and energetically advantageous process. These theoretical findings support the idea of chemisorption and the development of a protective molecular barrier on the steel surface because they are in perfect agreement with the electrochemical data. Additionally, molecular docking studies demonstrated the molecule's high affinity for binding to a variety of biological targets, indicating the possibility of multi-target pharmacological action. These interactions were varied, consistent, and frequently better than those of common reference medications. Favourable oral bioavailability, high intestinal absorption, minimal risk of cytochrome-mediated metabolism and transporter interactions, and non-mutagenicity

were all revealed by complementary ADME/toxicity predictions. Crucially, the compound did not exhibit any acute systemic toxic effects or the anticipated cardiotoxic effects. The suggestion of possible hepatotoxicity, however, emphasises the necessity of additional biological confirmation prior to any pharmacological advancement. For the development of 2-methyl-5-(2-methyl-1H-benzimidazol-5-yl)-1,3,4-oxadiazole as a dual-purpose material with promising corrosion inhibition and bioactivity profiles, this integrative study combining synthetic chemistry, electrochemical evaluation, molecular simulations (MD and MC), and in silico pharmacokinetics/toxicity offers a strong framework.

Acknowledgements

The authors are grateful to for the research assistance from Bioorganic Chemistry Team, Laboratory of Bioorganic Chemistry, Faculty of Sciences, Chouaib Doukkali University, 24000 El Jadida, Morocco and Molecular Modeling and Spectroscopy Research Team, Faculty of Science, Chouaib Doukkali University, P.O. Box 20, 24000 El Jadida, Morocco and Laboratory of Organic Chemistry, Bioorganic and Environment, Chemistry Department, Faculty of Sciences, Chouaib Doukkali University, El Jadida, Morocco

References

1. Elhady O. M., Mansour E. S., Elwassimy M. M., Zawam, S. A., and Drar A. M. (2022) Synthesis and characterization of some new tebufenozide analogues and study their toxicological effect against *Spodoptera littoralis* (Boisd.). *Curr Chem Lett.*, 11(1) 63-68.
2. El Tabl A., Zawam S., and Sarhan, K. (2021) Innovating new methods for wastewater treatment in El-Dakhla Oasis in Upper Egypt from chemical and biological pollutants using modified down Flow Hanging Sponge (DHS) reactor in presence of new environmental friendly chelator. *Egypt. J. Chem.*, 64(9) 4985-4994.
3. Elhady O. M., Erian S. M., Elwassimy M. M., Sameh A. Z., Drar A. M., and Shaban A. A. A. (2022) Selective synthesis, characterization, and toxicological activity screening of some furan compounds as pesticidal agents, *Curr Chem Lett.*, 11(3) 285-290
4. Al-Mulla A. (2017) A review: biological importance of heterocyclic compounds. *Der Pharma Chem.*, 9(13) 141-147.
5. Pace A., and Pierro P. (2009) The new era of 1, 2, 4-oxadiazoles. *Org. Biomol. Chem.*, 7(21) 4337-4348.
6. Boström J., Hogner A., Llinàs A., Wellner E., and Plowright A. T. (2012) Oxadiazoles in medicinal chemistry. *J. Med. Chem.*, 55(5) 1817-1830.
7. Delaugerre C. (2010) Genetic barrier to antiretroviral drug-resistance. Focus on raltegravir, the first integrase inhibitor. *Med. Mal. Infect.*, 40(2010) 1-10.
8. Sultana R., Ali A., Rana M., Ahmad I., Kamthan M., Almuqdad H. T. A., Mehendi R., Abid M., and El-Bahy, Z. M. (2024) Synthesis of oxadiazole derivatives: Anti-bacterial, DNA binding and in silico molecular modelling approaches. *J. Mol. Struct.*, 1318(2024) 139350.
9. James N. D., and Growcott J. W. (2009) Zibotentan. *Drug Future.*, 34(8) 624
10. Banerjee A. G., Das N., Shengule S. A., Srivastava R. S., and Shrivastava S. K. (2015) Synthesis, characterization, evaluation and molecular dynamics studies of 5, 6-diphenyl-1, 2, 4-triazin-3 (2H)-one derivatives bearing 5-substituted 1, 3, 4-oxadiazole as potential anti-inflammatory and analgesic agents. *Eur. J. Med. Chem.*, 101(2015) 81-95.
11. Gulnaz A. R., Mohammed Y. H. E., and Khanum S. A. (2019) Design, synthesis and molecular docking of benzophenone conjugated with oxadiazole sulphur bridge pyrazole pharmacophores as anti inflammatory and analgesic agents. *Bioorg. Chem.*, 92(2019) 103220.
12. Abd-Ellah H. S., Abdel-Aziz M., Shoman M. E., Beshr E. A., Kaoud T., and Ahmed A. S. F. (2017) New 1, 3, 4-oxadiazole/oxime hybrids: Design, synthesis, anti-inflammatory, COX inhibitory activities and ulcerogenic liability. *Bioorg. Chem.*, 74(2017) 15-29.
13. Jayashankar B., Rai K. L., Baskaran N., and Sathish H. S. (2009) Synthesis and pharmacological evaluation of 1, 3, 4-oxadiazole bearing bis (heterocycle) derivatives as anti-inflammatory and analgesic agents. *Eur. J. Med. Chem.*, 44(10) 3898-3902.
14. Kaur J., Soto-Velasquez M., Ding Z., Ghanbarpour A., Lill M. A., van Rijn R. M., Watts V. J., and Flaherty D. P. (2019) Optimization of a 1, 3, 4-oxadiazole series for inhibition of Ca²⁺/calmodulin-stimulated activity of adenylyl cyclases 1 and 8 for the treatment of chronic pain. *Eur. J. Med. Chem.*, 162(2019) 568-585.
15. Tantray M. A., Khan I., Hamid H., Alam M. S., Dhulap A., and Kalam A. (2018) Synthesis of benzimidazole-linked-1,3,4-oxadiazole carboxamides as GSK-3 β inhibitors with in vivo antidepressant activity. *Bioorg. Chem.*, 77(2018) 393-401.
16. Singh P., Sharma P. K., Sharma J. K., Upadhyay A., and Kumar N. (2012) Synthesis and evaluation of substituted diphenyl-1, 3, 4-oxadiazole derivatives for central nervous system depressant activity. *org. Med. Chem. Lett.*, 2(8) 1-10.
17. Yadagiri B., Gurralla S., Bantu R., Nagarapu L., Polepalli S., Srujana G., and Jain N. (2015) Synthesis and evaluation of benzosuberone embedded with 1, 3, 4-oxadiazole, 1, 3, 4-thiadiazole and 1, 2, 4-triazole moieties as new potential anti proliferative agents. *bioorg. Med. Chem. Lett.*, 25(10) 2220-2224.
18. Glomb T., Szymankiewicz K., and Świątek P. (2018) Anti-cancer activity of derivatives of 1, 3, 4-oxadiazole. *Mol.*, 23(12) 3361.

19. Shyma P. C., Balakrishna K., Peethambar K. S., and Vijesh M. A. (2015) Synthesis, characterization, antidiabetic and antioxidant activity of 1, 3, 4-oxadiazole derivatives bearing 6-methyl pyridine moiety. *Der Pharma Chem.*, 7(12) 137-45.
20. Nazreen S., Alam M. S., Hamid H., Yar M. S., Shafi S., Dhulap A., Alam P., Pasha M. A. Q., Bano S., Alam M. M., Haider S., Ali Y., Kharbanda C., and Pillai K. K. (2014) Design, synthesis, in silico molecular docking and biological evaluation of novel oxadiazole based thiazolidine-2, 4-diones bis-heterocycles as PPAR- γ agonists. *Eur. J. Med. Chem.*, 87(2014) 175-185.
21. Şahin G., Palaska E., Ekizoğlu M., and Özalp M. (2002) Synthesis and antimicrobial activity of some 1, 3, 4-oxadiazole derivatives. *Il Farmaco.*, 57(7) 539-542.
22. Ali M. A., and Shaharyar M. (2007) Oxadiazole mannich bases: Synthesis and antimycobacterial activity. *bioorg. Med. Chem. Lett.*, 17(12) 3314-3316.
23. Rane R. A., Bangalore P., Borhade S. D., and Khandare P. K. (2013) Synthesis and evaluation of novel 4-nitropyrrole-based 1, 3, 4-oxadiazole derivatives as antimicrobial and anti-tubercular agents. *Eur. J. Med. Chem.*, 70(2013) 49-58.
24. Zoumpoulakis P., Camoutsis C., Pairas G., Soković M., Glamočlija J., Potamitis C., and Pitsas, A., (2012) Synthesis of novel sulfonamide-1, 2, 4-triazoles, 1, 3, 4-thiadiazoles and 1, 3, 4-oxadiazoles, as potential antibacterial and antifungal agents. Biological evaluation and conformational analysis studies. *bioorg. Med. Chem.*, 20(4) 1569-1583.
25. Xu W., He J., He M., Han F., Chen X., Pan Z., Wang J., and Tong M. (2011) Synthesis and antifungal activity of novel sulfone derivatives containing 1, 3, 4-oxadiazole moieties. *Mol.*, 16(11) 9129-9141.
26. Johns B. A., Weatherhead J. G., Allen S. H., Thompson J. B., Garvey E. P., Foster S. A., Jeffrey J. L., and Miller W. H. (2009) 1, 3, 4-Oxadiazole substituted naphthyridines as HIV-1 integrase inhibitors. Part 2: SAR of the C5 position. *bioorg. Med. Chem. Lett.*, 19(6) 1807-1810.
27. El-Sayed W. A., El-Essawy F. A., Ali O. M., Nasr B. S., Abdalla M. M., and Abdel-Rahman A. A. H. (2009) Anti-HIV activity of new substituted 1, 3, 4-oxadiazole derivatives and their acyclic nucleoside analogues. *Z. Naturforsch. C.*, 64(11-12) 773-778.
28. Lipinski C. A. (2000) Drug-like properties and the causes of poor solubility and poor permeability. *J. Pharmacol. Toxicol. Methods.*, 44(1) 235-249.
29. Pires D. E., Blundell T. L., and Ascher D. B. (2015) pkCSM: predicting small-molecule pharmacokinetic and toxicity properties using graph-based signatures. *J. Med. Chem.*, 58(9) 4066-4072.
30. Morris G. M., Huey R., Lindstrom W., Sanner M. F., Belew R. K., Goodsell D. S., and Olson A. J. (2009) AutoDock4 and AutoDockTools4: Automated docking with selective receptor flexibility. *J. Comput. Chem.*, 30(16) 2785-2791.
31. Trott O., and Olson A. (2009) Software news and update AutoDock Vina: Improving the speed and accuracy of docking with a new scoring function. *Effic. Optim. Multithreading*, 31(2) 455-461.
32. Lyapustin D. N., Fayzullina D. F., Marusich I. V., Kotovskaya S. K., Melekhin, V. V., Tokhtueva M. D., Ulomsky E. N., and Rusinov, V. L. (2024) A synthesis of novel 5-methylsulfanylazolo [1, 5-a] pyrimidin-7 (4 H)-ones and investigation of their chemical and cytotoxic properties. *Chem. Heterocycl. Compd.*, 60(1) 52-57.
33. Pavlinac I. B., Starčević K., Persoons L., Banjanac M., Radovanović V., Daelemans D., and Hranjec M. (2024) Novel iminocoumarin imidazo [4, 5-b] pyridine derivatives: design, synthesis, and biological evaluation. *Chem. Heterocycl. Compd.*, 60(1) 75-82.
34. Loskutov O. A., Melnykov K. P., Ryabukhin S. V., Rusanov E. B., Chaikovskiy I. A., Khavryuchenko O. V., Dziuba D. O., and Volochnyuk, D. M. (2024) Thiazolo [5, 4-b] indole derivatives as additives to cardioplegic solutions with increased time of preventing hypothermic ischemia. *Chem. Heterocycl. Compd.*, 60(1) 83-91.
35. Sadowski M., and Kula K. (2024) Unexpected course of reaction between (1E, 3E)-1, 4-Dinitro-1, 3-butadiene and n-methyl azomethine ylide—a comprehensive experimental and quantum-chemical study. *Molecules*, 29(21) 5066.
36. Kaul S., Kumar A., Sain B., and Bhatnagar A. K. (2007) Simple and convenient one-pot synthesis of benzimidazoles and benzoxazoles using N, N-Dimethylchlorosulfitemethaniminium chloride as condensing agent. *Synth. Commun.*, 37(15) 2457-2460.
37. Phillips M. A. (1928) CCCXVII.—The formation of 2-substituted benziminazoles. *J. Chem. Soc.*, 2393-2399.
38. Galal S. A., Hegab K. H., Kassab A. S., Rodriguez M. L., Kerwin S. M., El-Khamry A. M. M. A., and El Diwani H. I. (2009) New transition metal ion complexes with benzimidazole-5-carboxylic acid hydrazides with antitumor activity. *Eur. J. Med. Chem.*, 44(4) 1500-1508.
39. Shekarchi M., Navidpour L., Khorami A. R., Partoazar A., Shafaroodi H., Rahmanipour N., and Shekarchi M. (2011) Synthesis of N-arylidene-2-(2-phenoxyphenyl) acetohydrazides as anti-inflammatory agents. *Iran. J. Pharm. Res.*, 10(2) 369.
40. Galal S. A., Hegab K. H., Kassab A. S., Rodriguez M. L., Kerwin S. M., El-Khamry A. M. M. A., and El Diwani H. I. (2009) New transition metal ion complexes with benzimidazole-5-carboxylic acid hydrazides with antitumor activity. *Eur. J. Med. Chem.*, 44(4) 1500-1508.
41. Yadav D., Bodke S., Biradar A., and Kenchappa R. (2016) Synthesis, characterization and biological evaluation of 2-(2-substituted)-5-phenyl-1, 3, 4-oxadiazole and 3, 6-diphenyl [1, 2, 4] triazole [3, 4][1, 3, 4] thiadiazole derivatives. *Indian J Adv Chem Sci.*, 4(2016) 269-275.
42. « Gaussian.com | Expanding the limits of computational chemistry ». Consulté le: 25 avril 2025. [En ligne]. Disponible sur: <https://gaussian.com/>

43. « Protein Data Bank | Nucleic Acids Research | Oxford Academic ». Consulté le: 22 avril 2025. [En ligne]. Disponible sur: <https://academic.oup.com/nar/article/28/1/235/2384399>
44. Kim S., Chen J., Cheng T., Gindulyte A., He J., He S., Li Q., Shoemaker B. A., Thiessen P. A., Yu B., Zaslavsky L., Zhang J., and Bolton, E. E. (2021) PubChem in 2021: new data content and improved web interfaces. *Nucleic Acids Res.*, 49(D1) D1388-D1395.
45. Morris G. M., Huey R., Lindstrom W., Sanner M. F., Belew R. K., Goodsell D. S., and Olson A. J. (2009) AutoDock4 and AutoDockTools4: Automated docking with selective receptor flexibility. *J. Comput. Chem.*, 30(16) 2785-2791.
46. Trott O., and Olson A. (2009) Software news and update AutoDock Vina: Improving the speed and accuracy of docking with a new scoring function. *Effic. Optim. Multithreading.*, 31(2) 455-461.
47. Fakhry H., El Faydy M., Benhiba F., Bouassiria M., Laabaissi T., Allali M., Touir R., Oudda H., Jama C., Warad I., Alsalmé A., and Zarrouk A. (2022) Experimental, DFT studies and molecular dynamic simulation on the corrosion inhibition of carbon steel in 1 M HCl by two newly synthesized 8-hydroxyquinoline derivatives. *J. Indian Chem. Soc.*, 99(12) 100701.
48. Benhiba F., Benzekri Z., Kerroum Y., Timoudan N., Hsissou R., Guenbour A., Belfaquir M., Boukhris S., Oudda H., and Zarrouk A. (2023) Assessment of inhibitory behavior of ethyl 5-cyano-4-(furan-2-yl)-2-methyl-6-oxo-1, 4, 5, 6-tetrahydropyridine-3-carboxylate as a corrosion inhibitor for carbon steel in molar HCl: Theoretical approaches and experimental investigation. *J. Indian Chem. Soc.*, 100(2) 100916.
49. El Faydy M., Benhiba F., Warad I., Saoiabi S., Alharbi A., Alluhaybi A. A., Lakhrissi, B., Abdallah M., and Zarrouk A. (2022) Bisquinoline analogs as corrosion inhibitors for carbon steel in acidic electrolyte: Experimental, DFT, and molecular dynamics simulation approaches. *J. Mol. Struct.*, 1265(2022) 133389.
50. Abd-El-Nabey B. A., Abdel-Gaber A. M., Elewady G. Y., Sadeek M. E., and Abd-El-Rhman H. (2012) Inhibitive action of benzaldehyde thiosemicarbazones on the corrosion of mild steel in 3 M H₃PO₄. *Int. J. Electrochem. Sci.*, 7(12) 11718-11733.
51. Berrissoul A., Ouarhach A., Benhiba F., Romane A., Guenbour A., Dikici B., Bentiss F., Zarrouk A., and Dafali A. (2022) Assessment of corrosion inhibition performance of origanum compactum extract for mild steel in 1 M HCl: Weight loss, electrochemical, SEM/EDX, XPS, DFT and molecular dynamic simulation. *Ind. Crop. Prod.*, 187(2022) 115310.
52. Belghiti M. E., Karzazi Y., Dafali A., Obot I. B., Ebenso E. E., Emran K. M., Bahadur I., Hammouti B., and Bentiss F. (2016) Anti-corrosive properties of 4-amino-3, 5-bis (disubstituted)-1, 2, 4-triazole derivatives on mild steel corrosion in 2 M H₃PO₄ solution: Experimental and theoretical studies. *J. Mol. Liq.*, 216(2016) 874-886.
53. Li X., Deng S., Xie X., and Du G. (2016) Synergistic inhibition effect of 5-aminotetrazole and 4, 6-dihydroxypyrimidine on the corrosion of cold rolled steel in H₃PO₄ solution. *Mater. Chem. Phys.*, 181(2016) 33-46.
54. Li X., Deng S., and Fu H. (2011) Synergistic inhibition effect of 6-benzylaminopurine and iodide ion on the corrosion of cold rolled steel in H₃PO₄ solution. *Corros. Sci.*, 53(11) 3704-3711.
55. Ech-Chihbi E., Nahlé A., Salim R., Benhiba F., Moussaif A., El-Hajjaji F., Oudda H., Guenbour A., Taleb M., Warad I., and Zarrouk A. (2020) Computational, MD simulation, SEM/EDX and experimental studies for understanding adsorption of benzimidazole derivatives as corrosion inhibitors in 1.0 M HCl solution. *J. Alloys Compd.*, 844(2020) 155842.
56. Tang M., Deng S., Du G., and Li X. (2023) Mikania micrantha extract/KI blend as a novel synergistic inhibitor for steel corrosion in concentrated H₃PO₄ solution. *Ind. Crop. Prod.*, 193(2023) 116237.
57. Ismail A. S., and Farag A. A. (2020) Experimental, theoretical and simulation studies of extracted crab waste protein as a green polymer inhibitor for carbon steel corrosion in 2 M H₃PO₄. *Surf. Interfaces.*, 19(2020) 100483.
58. Al-Bonayan A. M. (2015) Inhibiting effect of thiosemicarbazide and 4-phenyl thiosemicarbazide towards the corrosion of carbon steel in H₃PO₄ solutions. *Int. J. Electrochem. Sci.*, 10(1) 589-601.
59. Benabdellah M., Hammouti B., Warthan A., Al-Deyab S. S., Jama C., Lagrenee M., and Bentiss F. (2012) 2, 5-Disubstituted 1, 3, 4-oxadiazole derivatives as effective inhibitors for the corrosion of mild steel in 2M H₃PO₄ solution. *Int. J. Electrochem. Sci.*, 7(4) 3489-3500.
60. Benhiba F., Sebbar N. K., Bourazmi H., Belghiti M. E., Hsissou R., Hökelek T., Bellaouchou A., Guenbour A., Warad I., Oudda H., Zarrouk A., and Essassi E. M. (2021). Corrosion inhibition performance of 4-(prop-2-ynyl)-[1, 4]-benzothiazin-3-one against mild steel in 1 M HCl solution: Experimental and theoretical studies. *Int. J. Hydrog. Energy.*, 46(51) 25800-25818.
61. Benabdellah M., Aouniti A., Dafali A., Hammouti B., Benkaddour M., Yahyi A., and Ettouhami A. (2006) Investigation of the inhibitive effect of triphenyltin 2-thiophene carboxylate on corrosion of steel in 2 M H₃PO₄ solutions. *Appl. Surf. Sci.*, 252(23) 8341-8347.
62. Hmamou D. B., Zarrouk A., Salghi R., Zarrok H., Ebenso E. E., Hammouti B., Kabanda M. M., Benchat N., and Benali O. (2014) Experimental and theoretical studies of the adsorption and corrosion inhibition of 6-phenylpyridazine-3 (2H)-thione on Carbon Steel in 2.0 M H₃PO₄ solution. *Int. J. Electrochem. Sci.*, 9(1) 120-138.



© 2025 by the authors; licensee Growing Science, Canada. This is an open access article distributed under the terms and conditions of the Creative Commons Attribution (CC-BY) license (<http://creativecommons.org/licenses/by/4.0/>).